4D image construction from free-breathing MRI slice acquisitions of the thorax based on a concept of flux

You Hao[1,2], **Jayaram K. Udupa**[2], **Yubing Tong**[2], **Caiyun Wu**[2], **Hua Li**[1], **Joseph M. McDonough**[3], **Drew A. Torigian**[2], **Patrick J. Cahill**[3]

[1]Key Laboratory of Intelligent Information Processing, Institute of Computing Technology, Chinese Academy of Sciences, Beijing 100190, China

[2]Medical Image Processing Group, 602 Goddard building, 3710 Hamilton Walk, Department of Radiology, University of Pennsylvania, Philadelphia, PA 19104, United States

[3]Center for Thoracic Insufficiency Syndrome, Children's Hospital of Philadelphia, Philadelphia, PA 19104, United States

Abstract

Retrospective 4D image construction from continuously acquired 2D slices is a necessary step to achieve high-quality 4D images. Self-gating methods, which extract breathing signals only from image information without any external gating technology, have much potential, such as in pediatric patients with thoracic insufficiency syndrome (TIS) who suffer from extreme malformations of the chest wall, diaphragm, and spine, leading to breathing that is very complex with lots of abnormal respiration cycles, including very deep or shallow cycles. Existing methods do not work well in this clinical scenario and most are not fully automatic, requiring some manual interactive operations. In this paper, we propose a fully automatic 4D dMRI construction method based on the concept of flux to address the 4D image construction from 2D slices of subjects with complex respiration. Firstly, we extract the breathing signal for each location based on the flux of the optical flow vector field of the body region from the image series. Then, we give a full analysis for all cycles and extract several normal ones and map them to one cosine respiration model for each location. After that, we re-sample one normal cycle from the respiration model for each location independently. All of these resampled normal cycles form the final constructed 4D image. Qualitative and quantitative evaluations on 25 subjects show that the proposed method can handle datasets from subjects with more complex respiration and achieves good self-consistency results while maintaining time and space continuity.

Keywords

4D construction; optical flux; dynamic MRI; thoracic insufficiency syndrome

1. INTRODUCTION

Respiratory organ motion analysis is important in the study of many disease processes [1]. In all such applications, a 4D image constituting the organ system under study needs to be constructed first. Compared to computed tomography (CT), magnetic resonance imaging (MRI) has three natural advantages: excellent soft tissue contrast, no ionizing radiation

exposure, and greater flexibility in selecting image plane position, orientation, and duration. Therefore, MRI-based 4D imaging technology is highly desirable in many clinical applications.

There are two main approaches to 4D image formation via MRI [2]: i) Using fast 3D MRI sequences to acquire real-time 3D volumetric data; and ii) Using fast 2D MRI sequences to continuously acquire 2D images from all respiratory phases, location by location spatially, then resorting these slices to form 4D images. For the real-time approach, limited by current hardware and software, it is difficult to achieve high spatial resolution while ensuring adequate temporal resolution and image quality. For the 2D approach, since the 3D structure is not maintained in 2D MRI sequences, some form of internal or external respiratory surrogate is required to restore the respiratory motion, which is the most important part of this approach.

However, the respiratory surrogate approaches are often subject to some drawbacks. To overcome these shortcomings, researchers have focused on methods of extracting motion signals based only on the scanned image series, which are known as self-gating methods. Such approaches can be grouped into 3 main categories: feature-based surrogate [2, 3, 4], graph-based optimization [5, 6], and manifold learning alignment [7, 8, 9, 10]. Yet, most of these strategies are not fully automatic or cannot deal with subjects with complex respiration cycles, which in the case of very sick pediatric patients becomes a major hurdle. In this paper, we present a fully automatic 4D dynamic MRI (dMRI) construction approach which by design tries to overcome the above hurdles. The approach centers around a novel concept we propose as a respiratory surrogate, called *flux*, and consists of three major steps: i) Respiratory signal extraction; ii) Extraction and analysis of cycles; and iii) Normal cycle construction and 4D image formation.

2. MATERIALS AND METHODS

2.1 Materials

In this paper, we utilize dMRI data sets from 25 pediatric subjects with no known thoracic anomalies. The scan data were obtained from the Children's Hospital of Philadelphia (CHOP) following approval from the Institutional Review Board at CHOP and the University of Pennsylvania along with a Health Insurance Portability and Accountability Act waiver. Each subject was scanned using the same imaging protocol from the right lateral end to the left lateral end of thorax under breathing conditions that are natural for the subject. The dMRI scan protocol was as follows: 3T MRI scanner (Siemens Healthcare, Erlangen, Germany), true-fast imaging with steady-state precession sequence; TR/TE = 3.82/1.91 msec; voxel size of approximately $1 \times 1 \times 6$ mm^3; $320 \times 320 \times 38$ matrix; bandwidth = 558 Hz; flip angle = 76°; and one signal average. For each of 30–40 sagittal plane locations through the thorax, slice data were obtained during 8–14 tidal breathing cycles at approximately 200 msec per slice; total acquisition time per subject = 40 minutes. This process yields over 2000–3000 slices in total for one patient and constitutes a spatio-temporal sampling of the subject's dynamic thorax over 240–560 respiratory cycles.

2.2   Optical flux

Optical flow is a commonly-used method to capture motion in computer vision. We estimate optical flow based on the body region, which reduces the impact of background noise from outside the body region influencing analysis within the body region. This idea is crucial for capturing the motion of lungs and hemi-diaphragms precisely. Two examples of optical flow estimated within the body region are shown in Figure 1. In Figure 1(a), the two time-adjacent slices are in the inspiration phase. The optical flow vector field in this case generally points towards the body region boundary overall, as shown in the figure. In Figure 1(b), the two time-adjacent slices are in the expiration phase, and as such the vector field points towards the inside as shown. From close scrutiny of all of the data sets, we observed that optical flow can capture the non-rigid local movement within the body region precisely.

Optical flow estimation from two successive slices in the time dimension yields a vector field. Divergence at a point P in this vector field is a local measure of "outgoingness" of vectors at P. In other words, it denotes the amount of outward flux locally within an infinitesimal volume around P. The total "outgoingness" for the body region, which we will term *optical flux*, is simply an integral of divergence over the body region. The divergence map for the optical flow vector field is shown in the Divergence part of Figure 1. Notably, on the one hand, the divergence at most pixels in Figure 1(a) is positive, as indicated by the temperature color scale. On the other hand, the divergence of most pixels in Figure 1(b) is negative, as depicted by the cold color palette. As we can see, the optical flux for the inspiration phase in Figure 1(a) is positive and that for the expiration phase in Figure 1(b) is negative.

In our application area of interest, namely pediatric thoracic insufficiency syndrome (TIS) [11], for each of 35–40 sagittal slice locations across the chest, 80 MRI slices are acquired rapidly (in 200–300 msec per slice) while the patient is undergoing free breathing over 10–12 cycles. Since all processing is done identically in this paper on the sequence of slices acquired for each sagittal location, we will confine our description to one fixed sagittal location z and represent the sequence of 80 slices acquired for z by $A_z = \{f_{T_1}, f_{T_2}, ..., f_{T_M}\}$. This constitutes a time sequence of slices. From each pair of successive time slices in the sequence, optical flow is estimated using the Lucas-Kanade method [12] within the body region inside the skin boundary. Optical flux is then derived by first performing a divergence operation on the flow vector field and integrating divergence within the body region. After estimating optical flux for each time point in A_z based on adjacent time slices in the sequence in this manner, we derive an optical-flux curve as shown in Figure 1(c), which can be regarded as the respiratory signal associated with this location z. Notably, optical flux can represent the respiratory signal accurately.

2.3   Analysis of cycles

With the motion captured with optical flux, we perform an analysis of the respiratory cycles whose goal is to output one normal cycle per z location. Firstly, we detect the End-Inspiration (EI) and End-Expiration (EE) points (Figure 2(a)) in A_z and extract all respiratory cycles included in A_z. If all respiratory cycles are near-normal as in the example in Figure 1(c), we can detect EI and EE points easily depending on the zero-crossings of the

flux curve. However, A_z typically contains abnormal patterns, as in the example in Figure 2. To detect EI and EE points, we first find all peaks on the flux curve and then filter out peaks with values close to 0. The final detected peaks are shown in Figure 2, represented by triangles. Then, following the time sequence, we find the last time point (slice) with positive flux after each peak as an EI point and the first slice with negative flux before each peak as an EE point. The detected EI-EE points are displayed in Figure 2(a).

There are typically 10–12 cycles at each z in our MRI data. Some of the cycles are normal, whereas others are abnormal (meaning very shallow or briefly stopped breathing or deep breathing).

With the detected cycles and flux curves, we make a deeper analysis of the cycles. We define several measurements to represent the character of cycles, such as the volume at inspiration, volume at expiration, the number of peaks and valleys on the flux curve, the distance between the peak point and the EI point, etc. We detect and filter out the abnormal cycles based on these measurements. We will use only the normal cycles to build the final single cycle to be associated with z, as shown in Figure 2(b).

2.4 Cycle construction

To construct one cycle for each z location, we should determine the hemi-diaphragm position as a function of time first. The physical meaning of flux is closely related to the lung's moving speed at any time point. So, we can get the relative distance of motion of the hemi-diaphragm depending on the amount of flux. With the diaphragm position, we can infer the time position (respiratory phase) of any time-slice in the normal cycle. Then we can align all slices of the normal cycles in A_z to a normal cycle model, as shown in Figure 3(a) where we use a cosine model. In other words, we map on to the model the phases of all accepted normal cycles. The red points in the figure represent the inspiration phases and the yellow dots represent the expiration phases. With this normal model, we can re-sample the normal cycle with any desired number of time points within limits. Then, by selecting the same number of time points, we can guarantee that the cycles at different z locations have the same phase and same number of time points in the 4D construction. In practice, we determine the mean number of time points over all normal cycles in A_z. Then we use that number as the number for resampling. The resampled cycle is shown in Figure 3(b) for the model cycle depicted in Figure 3(a). At each z location, we will thus get one re-sampled normal cycle. The cycles from all locations will form the final 4D constructed volume of the dynamic thorax.

3. EXPERIMENTS AND RESULTS

We tested our method on dMRI data sets from 25 normal subjects. To evaluate the accuracy of the construction results, we focus on both temporal and spatial continuity of the constructed 4D image.

3.1 Temporal continuity

The first test is for assessing temporal continuity. This metric defines the number of time instances in a cycle that are out of cyclic order as a fraction of the total number of time

instances in the cycle, which can be termed as Error in Temporal Order (E_{to}). In the examples shown in Figure 4, all cycles have 6 time points in the cycle, the cycles in (a) and (b) have all of their time intervals in the proper cyclic order, hence $E_{to} = 0$, and the cycles in (c) and (d) have 1 interval out of order – 6th interval in (c) and 1st interval in (d) – and thus $E_{to} = 1/6$ for these cycles.

Figure 5 summarizes E_{to} values over all data sets. The mean and standard deviation of E_{to} over all 25 data sets in our study are found to be 2.7% ± 2.3%.

3.2 Spatial continuity

This metric defines spatial smoothness in the z dimension of the constructed 4D image. For each time-instance of the 4D image, we select one point at the middle of the hemi-diaphragm dome manually. These points will form a curve as a function of z. The smoothness of this curve reflects the spatial continuity quality along z of our 4D constructed image. To quantify this smoothness, we first fit a spline function to the curve and then use the mean of the absolute distance from the labeled points to the fitted curve as the spatial smoothness factor for that time point, which can be termed as Error of Spatial Smoothness (E_{ss}). Two examples are shown in Figure 6 for one time-instance: (a) with $E_{ss} = 0.226$, and (b) with $E_{ss} = 2.422$ (both in pixel units). The mean and standard deviation of E_{ss} values over all data sets in our study are found to be 0.50 ± 0.17 pixel units.

In addition, to evaluate the spatial continuity subjectively, we use a spatial smoothness score for this purpose. We manually assess the spatial smoothness by examining each spatial 3D volume and assigning a subjective score on a 1–5 scale (1 = poor, 5 = perfect). The score is determined for each time point by visualizing all z-location slices and checking the smoothness of both hemi-diaphragm regions, which can be termed as Error of Spatial Continuity (E_{sc}). Figure 7 displays the mean of E_{sc} values over all time instances for each constructed 4D image over all data sets. The mean and standard deviation of E_{sc} values over all data sets in our study are found to be 4.6 ± 0.48.

We note that our approach achieves remarkable spatial and temporal continuity for all subjects. Over all tested data sets and cycles, temporal disorderliness is less than 0.1! The two smoothness scores (subjective and automatically determined) are in perfect agreement as seen from the red and blue curves in Figure 7. The objective smoothness factor is less than 1-pixel unit for all subjects! Finally, in Figure 8, we present exemplary slices from a constructed 4D image of a normal subject.

4. CONCLUSION

In this paper, we proposed a novel automatic 4D construction method for dynamic MRI of the thorax based on the concept of *flux*. The construction procedure is independent of the number of z-locations, which implies that it can be employed even when imaging is done with only a few sagittal locations and not the full set across the chest. The most important contribution of the method is that all procedures are fully automatic while not sacrificing robustness to other impediments such as abnormal breathing patterns. The method is general, i.e., not specific to the dMRI application illustrated in this work, and is independent

of the imaging protocol. For example, it can be readily applied to any other dMRI protocol and even dynamic computed tomography (CT) acquisitions without modification. With some changes, it can also be applied to other dynamic and moving organs such as heart, upper airway, and abdominal structures, amongst others.

ACKNOWLEDGMENTS

REFERENCES

[1]. Crompton G, "A brief history of inhaled asthma therapy over the last fifty years," Primary care respiratory journal 15(6), 326 (2006).

[2]. Cai J, Chang Z, Wang Z, Paul Segars W, and Yin F-F, "Four-dimensional magnetic resonance imaging (4D-MRI) using image-based respiratory surrogate: a feasibility study," Medical physics 38(12), 6384–6394 (2011). [PubMed: 22149822]

[3]. Liu Y, Yin F-F, Chang Z, Czito BG, Palta M, Bashir MR, Qin Y, and Cai J, "Investigation of sagittal image acquisition for 4D-MRI with body area as respiratory surrogate," Medical physics 41(10) (2014).

[4]. Yang J, Cai J, Wang H, Chang Z, Czito BG, Bashir MR, and Yin F-F, "Four-dimensional magnetic resonance imaging using axial body area as respiratory surrogate: initial patient results," International Journal of Radiation Oncology* Biology* Physics 88(4), 907–912 (2014).

[5]. Tong Y, Udupa JK, Ciesielski KC, Wu C, McDonough JM, Mong DA, and Campbell RM Jr, "Retrospective 4D MR image construction from free-breathing slice acquisitions: A novel graph-based approach," Medical image analysis 35, 345–359 (2017). [PubMed: 27567735]

[6]. Romaguera LV, Olofsson N, Plantefève R, Lugez E, De Guise J, and Kadoury S, "Automatic self-gated 4D-MRI construction from free-breathing 2Ds acquisitions applied on liver images," International Journal of Computer Assisted Radiology and Surgery, 1–12 (2019).

[7]. Baumgartner CF, Kolbitsch C, Balfour DR, Marsden PK, McClelland JR, Rueckert D, and King AP, "High-resolution dynamic MR imaging of the thorax for respiratory motion correction of pet using groupwise manifold alignment," Medical image analysis 18(7), 939–952 (2014). [PubMed: 24972374]

[8]. Baumgartner CF, Gomez A, Koch LM, Housden JR, Kolbitsch C, McClelland JR, Rueckert D, and King AP, "Self-aligning manifolds for matching disparate medical image datasets," in International Conference on Information Processing in Medical Imaging, 363–374, Springer (2015).

[9]. Uh J, Khan MA, and Hua C, "Four-dimensional MRI using an internal respiratory surrogate derived by dimensionality reduction," Physics in Medicine & Biology 61(21), 7812 (2016). [PubMed: 27754983]

[10]. Clough JR, Balfour DR, Marsden PK, Prieto C, Reader AJ, and King AP, "MRI slice stacking using manifold alignment and wave kernel signatures," in 2018 IEEE 15th International Symposium on Biomedical Imaging (ISBI 2018), 319–323, IEEE (2018).

[11]. Tong Y, Udupa JK, McDonough JM, Wileyto EP, Capraro A, Wu C, Ho S, Galagedera N, Talwar D, Mayer OH, Torigian DA, and Campbell RM, "Quantitative dynamic thoracic MRI: application to thoracic insufficiency syndrome in pediatric patients," Radiology 292(1), 206–213 (2019). [PubMed: 31112090]

[12]. Barron JL, Fleet DJ, Beauchemin SS, "Performance of optical flow techniques". International Journal of Computer Vision. 12(1), 43–77 (1994).
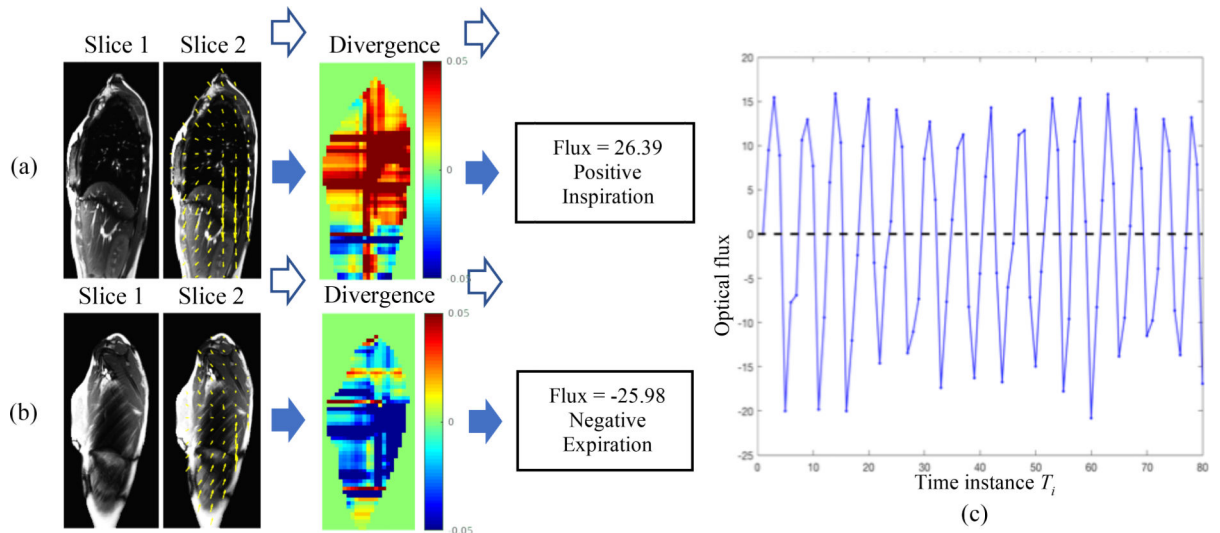
Figure 1:
Two examples of optical flow within the body region: (a) Two slices in the inspiration phase. (b) Two slices in the expiration phase. (c) Optical flux curve derived from 80 time-slices at one z location.
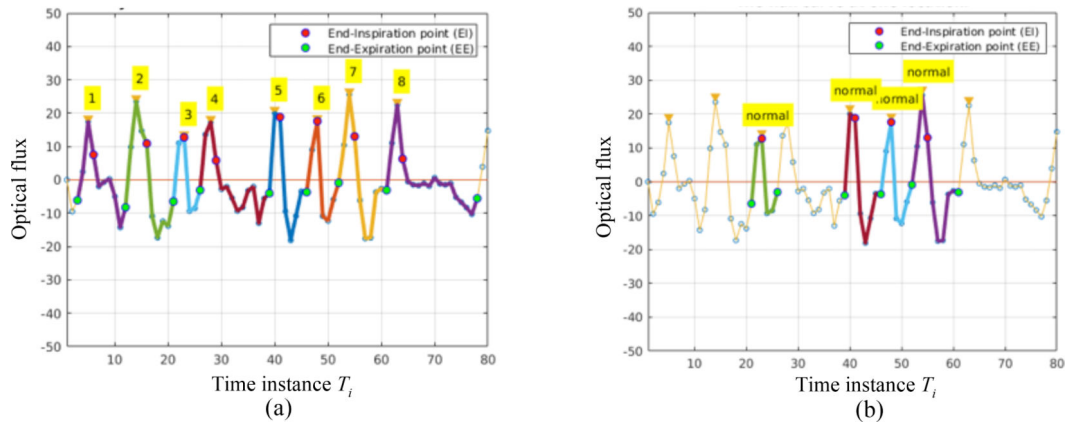
Figure 2:
(a) The cycles detected based on optical-flux curve at one z location. (b) The detected normal cycles are shown in bold.
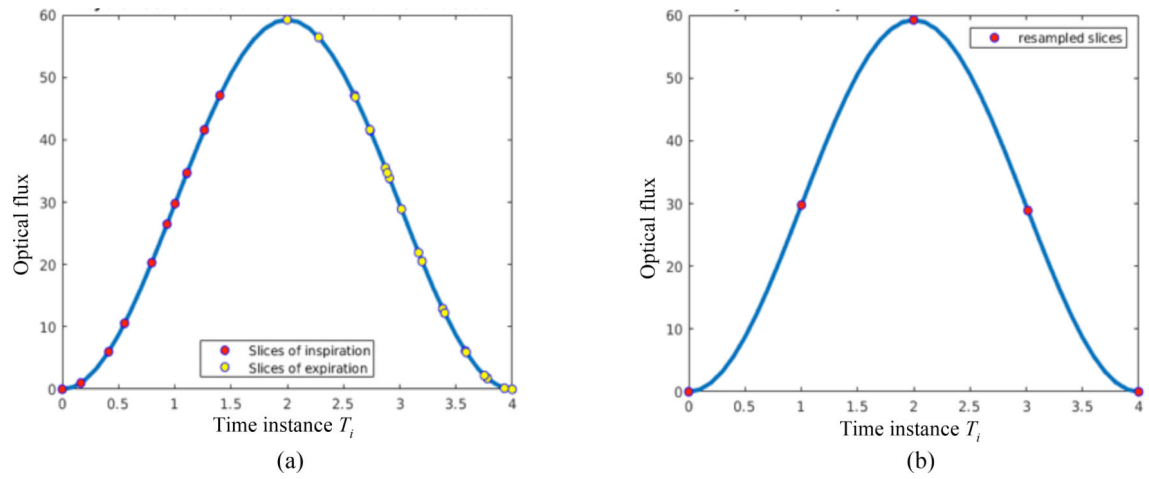
Figure 3:
Cycle construction. (a) A cosine model of the respiratory cycle on to which the time slices of the detected normal cycles are mapped. (b) A single normal cycle resampled from the model and time points shown in (a).
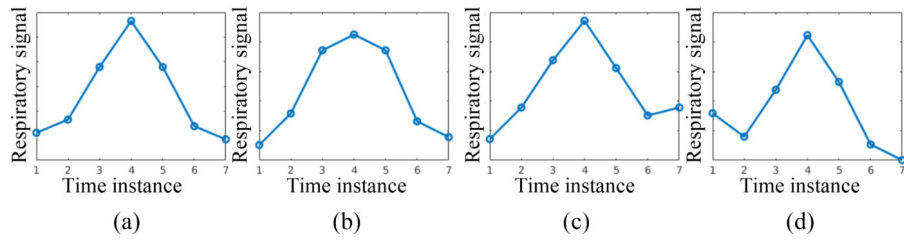
Figure 4:
Examples of temporal order/ disorder. The cycles in (a) and (b) are in cyclic order. The cycle is out of order at 6th time interval in (c) and at 1st time interval in (d).
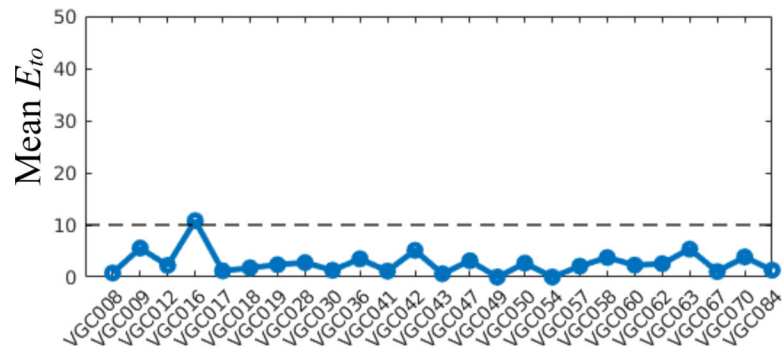
Figure 5:
Error in temporal order (E_{to}). Mean value of E_{to} over the cycles over all data sets.

(a) (b)
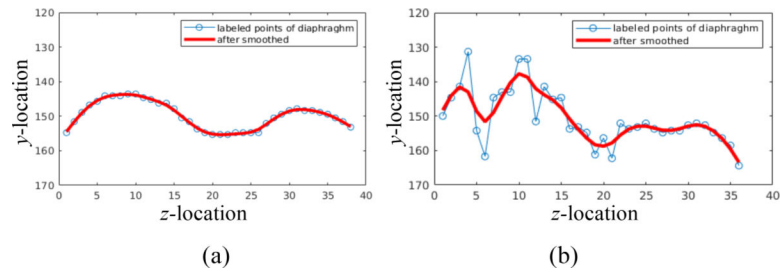
Figure 6:
Pattern of change in the y-location of the mid-point in the right and left hemi-diaphragm domes: An example of a spatially smooth (a) and non-smooth (b) construction.
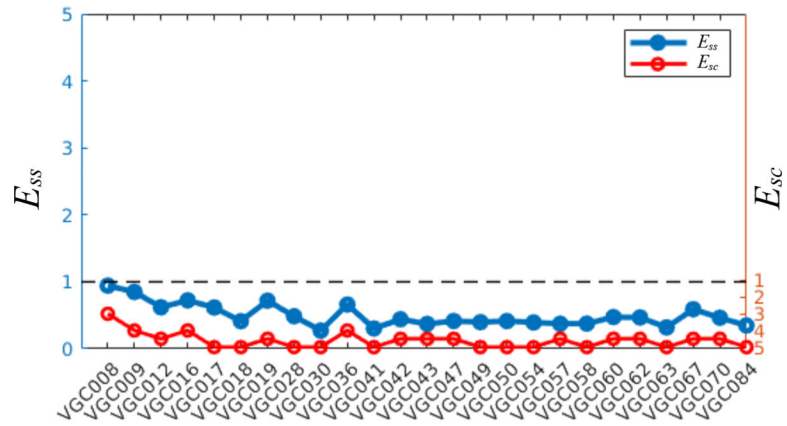
Figure 7:

Degree of spatial smoothness. Mean of E_{ss} values (blue) and E_{sc} values (red) over all time instances in the constructed 4D image over all data sets.
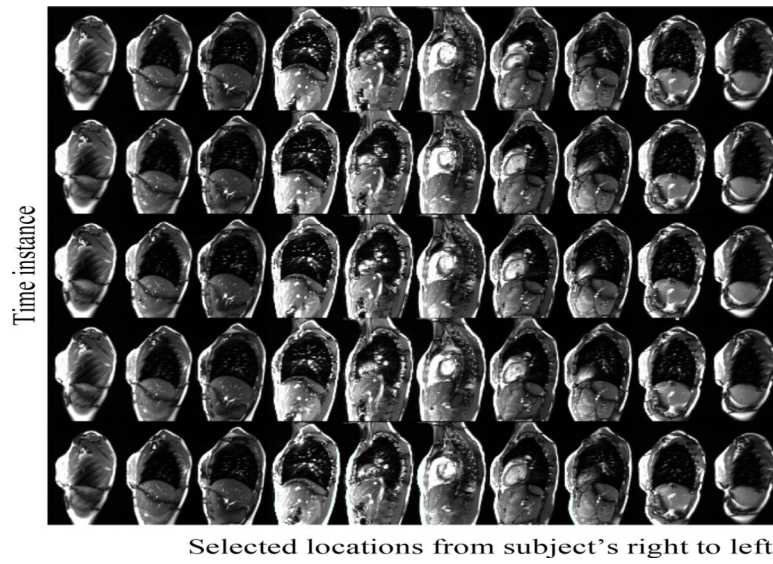
Figure 8:
A display of sagittal thoracic MRI slices selected from a constructed 4D image of a normal pediatric subject. Each column represents a *z*-location, and each row represents a time instance.